Auton Robot (2010) 28: 213–230
DOI 10.1007/s10514-009-9163-6

Experimental test of a robust formation controller for marine unmanned surface vessels

Daniel Schoerling · Chris Van Kleeck · Farbod Fahimi · Charles Robert Koch · Alfons Ams · Peter Löber

Received: 29 May 2009 / Accepted: 10 November 2009 / Published online: 3 December 2009

Abstract Experiments with two formation controllers for marine unmanned surface vessels are reported. The formation controllers are designed using the nonlinear robust model-based sliding mode approach. The marine vehicles can operate in arbitrary formation configurations by using two leader-follower control schemes. For the design of these controller schemes 3 degrees of freedom (DOFs) of surge, sway, and yaw are assumed in the planar motion of the marine surface vessels. Each vessel only has two actuators; therefore, the vessels are underactuated and the lack of a kinematic constraint puts them into the holonomic system category. In this work, the position of a control point on the vessel is controlled, and the orientation dynamics is not directly controlled. Therefore, there is a potential for an oscillatory yaw motion to occur. It is shown that the orientation dynamics, as the internal dynamics of this underactuated system, is stable, i.e., the follower vehicle does not oscillate about its control point during the formation maneuvers. The proposed formation controller relies only on the state information obtained from the immediate neighbors of the vessel and the vessel itself. The effectiveness and robustness of formation control laws in the presence of parameter uncertainty and environmental disturbances are demonstrated by using both simulations and field experiments. The experiments were performed in a natural environment on a lake using a small test boat, and show robust performance to parameter uncertainty and disturbance. This paper reports the first experimental verification of the above mentioned approach, whose unique features are the use of a control point, the zero-dynamic stability analysis, the use of leader-follower method and a nonlinear robust control approach.

Keywords Formation control · Autonomous vehicles · Marine vehicles · Surface vessels · Sliding mode control · Experimental verification

D. Schoerling · C. Van Kleeck · F. Fahimi (✉) · C.R. Koch
University of Alberta, Edmonton, Canada
e-mail: fahimi@eng.uah.edu

A. Ams · P. Löber
Technische Universität Bergakademie Freiberg, Freiberg, Germany

1 Introduction

Military and civilian applications of marine unmanned surface vessels are growing. Many of these applications are for surveillance, which require full-time service of the vehicles. Currently, unmanned surface vessels are prodominantly controlled remotely by humans. There is a need for an autonomous controller to operate these vessels continuously with minimum human interaction, thus allowing humans to perform high-level supervision of more vessels in operation. The goal of this research is to provide and prove a method for autonomous control of multiple unmanned surface vessels.

Most of the deployed unmanned surface vessels are not fully actuated due to weight, reliability, complexity, and efficiency considerations. Controlling underactuated vehicles is especially challenging because they are not fully feedback linearizable and show nonholonomic constraints, so standard tools to control nonlinear systems—such as feedback linearization and integrator backstepping—may cause poor performance (Aguiar and Hespanha 2003). Currently, the applied control schemes vary from rudimentary proportional—derivative designs (Fossen 1994) over fuzzy control (Vaneck 1997; Gyoungwoo et al. 2009), linear quadratic Gaussian control (Naeem et al. 2008) to nonlinear control theories such as sliding-mode (Ashrafiuon et

al. 2008) and model predictive control (MPC) (Naeem et al. 2005).

Previous works cited above aimed to control the center of gravity of the surface vessel, which is not the most suitable approach for an underactuated vehicle. The concept of a control point for controlling underactuated speed boats with two independent thrusters was first introduced in Fahimi (2007a) and then used in Fahimi (2007b). In the control point approach, the controller aims to control the position of a control point instead of the position of the center of gravity. This control mechanism has the advantage that it indirectly stabilizes the heading angle. Performing a zero-dynamics analysis shows that the unactuated degree of freedom, i.e., the heading angle of the vessel, is stable. A practical zero-dynamics stability analysis for common boats is presented in this paper for the first time, to our knowledge. The concept of the control point is first brought to an experimental test in this research.

The state of the art of linearized control approaches for autonomous surface vessels is summarized in Fossen (1994). Traditionally trajectory tracking controllers have been designed using a two step methodology. First, a controller is designed to stabilize the vehicle dynamics. Second, an outer loop is designed that relies on the vehicle's kinematic model and converts trajectory tracking error into inner loop commands (Alves et al. 2006). The majority of the currently used inner loop controllers rely on linearized models using PID control (Roberts 2008). However, the quality of performance of a linearized model and the stability of linear control theories is provable only in the vicinity of the linearization state.

To overcome these limitations, numerous researchers have implemented more advanced and sophisticated control schemes. A way point following fuzzy controller was developed (Vaneck 1997). This controller does not require a complex mathematical model of the vehicle's dynamics. A fuzzy controller which controls the heading and brings the path of the vessel to the desired level was introduced in Gyoungwoo et al. (2009). Other approaches are using either linear or adaptive linear quadratic optimal control (Fossen 1994; Naeem et al. 2008). Most research focus has been on trajectory tracking controllers based on the nonlinear dynamic vessel model (Aguiar and Hespanha 2003; Ashrafiuon et al. 2008; Pettersen and Egel 1997; Indiveri and Aicardi 2000; Pettersen and Nijmeijer 1998; Encarnacao and Pascoal 2001; Behal et al. 2000). The focus of this research, however, is on formation control for multiple vessels rather than the trajectory-tracking control for a single vessel.

Formation control is a subcategory of controlling autonomous surface vessels. In formation control, a group of cooperative vehicles must keep some user-defined distanced to each other while performing a maneuver. The approaches of formation control can be roughly categorized under either behavior-based (Balch and Arkin 1998; Duman and Hu 2001), virtual structures (Lewis and Tan 1997), or leader-follower approaches (Fahimi 2007a, 2007b; Sugar and Kumar 1998; Desai 2002; Fahimi et al. 2008). In the leader-follower approach, a follower is designated to track the position and orientation of a leader with some prescribed offset. The leader can be either a real vessel or a virtual vessel following a trajectory determined by a global path planner. Different variations of this approach have been introduced in the field of mobile robots (Desai 2002), intelligent highways (Sheikholeslam and Desoer 1992), space vehicles (Kapila et al. 1992), helicopters (Fahimi 2008), and marine vessels (Fahimi 2007a).

This paper presents the design and experimental test of a nonlinear model-based sliding-mode formation controller for an unmanned surface vessel using the leader-follower approach. The approach presented in Fahimi (2007a) is highly customized and implemented on a test vessel, which has a significantly different drive-train than what was previously considered. General trajectories are considered for the leader(s) of the formation. The controller presented in this paper is derived based on a nonlinear dynamic model describing boats and ships. This model is used for all common naval applications such as tankers, cargo ships, and cruise ships, and is controlled by changing the propeller speed and rudder angle.

As autonomous underactuated surface vessels are a subject of active research, many researchers have performed tests to prove different control schemes. For instance, tests of a proposed sliding-mode controller has been performed in a small indoor pool in the absence of disturbances and by using a camera for navigation (Ashrafiuon et al. 2008). The usage of a gain-scheduled controller for a surface vessel on the sea was shown in Alves et al. (2006) and test results of a fuzzy controlled surface vessel are provided in Vaneck (1997). The path of the fuzzy controlled boat in between given way points is undetermined. The tests presented in this paper are different because the tests are performed outdoors on a large lake with significant disturbances for different common trajectories (straight line, circular motion, and zigzag motion) and the surface vessel (total mass 7.8 kg) has to follow the (virtual) leader vessels with a prescribed offset at all times. For guidance and navigation, a state measurement unit including, accelerometers, gyroscopes, a magnetometer, and a GPS receiver are used. The disturbances (wind, waves, and current) can reach approximately a maximum of up to 45% of the maximum driving force of the surface vessel. Small boats are harder to stabilize due to smaller inertia and are exposed to larger ratios between disturbance force and driving force than large boats and ships; therefore, the proposed and tested controller should be more easily applied to larger boats and ships.

In summary, the contributions of this research are: its focus on formation control rather than trajectory-tracking control of marine surface vessels, the use of nonlinear model-based controller design, the use of a control point on the vessel as a control reference rather than its center of gravity (which leads to a stable zero-dynamics for the vessel's yaw motion), a zero-dynamic stability analysis, and finally outdoor tests with continuous maneuvers in harsh water conditions compared to the size of the test boat.

2 Experimental setup

The main components of the autonomous test vessel are presented in Fig. 1. The hardware used for the experiment consists of the components that make up the control box and the actuators of the boat. The control box, has the following three parts: a navigational sensor unit, an embedded control computer with a PC/104 form factor, and a servo switch card. The following sections explain the vessel's hardware and software with more details.

2.1 Hardware

The sensor unit is composed of three accelerometers, three rate gyroscopes, a magnetometer, and a WAAS capable GPS receiver. The data of the named sensors is then fused using a proprietary filtering technique (Rotomotion, LLC) to output the current state of the vessel. The state of the vessel is sent via a network/Ethernet port to a control computer. Both the sensor and the control computer are on-board of the unmanned vessel and have a wired network link.

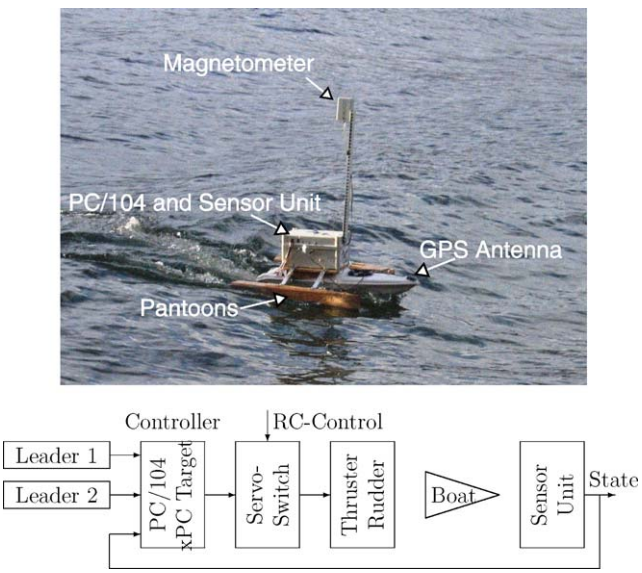

Fig. 1 Hardware setup of autonomous vessel (mass 7.8 kg, length 80 cm)

An embedded computer is used for control calculations. The embedded control computer has a compact PC/104 form factor and bus layout, specifically designed for embedded applications. The embedded computer features a Pentium M CPU 1.8 Ghz, 1 GByte DDR-RAM, and a 40 GByte HDD. The PC/104 computer transfers the control commands to a servo switch card (SSC) via serial communication.

The SSC allows the operator to switch between manual and computer control of the vessel and is triggered using a standard radio control (RC) receiver. The SSC also converts the serial signals from the PC/104 computer into PWM signals. Thus the output from this component is PWM regardless of the input source, either from the RC receiver, or from the PC/104 computer.

To provide the necessary motive force and control of the vessel a standard RC servo is used to change the propellers angle and a RC speed controller (a common open-loop one-quadrant drive controller) is used to set the motor speed, thus physically actuating the controller inputs $[n, \alpha]$. The motors drive two fixed blade propellers. The relationship between the pulse width I and the drive speed n in rps is

$$I = -0.0002 \cdot n^3 + 0.03 \cdot n^2 - 2.66 \cdot n + 1528. \tag{1}$$

For the steering servo the relationship between the pulse width I and the angle α in degree is

$$I = 16.25 \cdot \alpha + 1506. \tag{2}$$

2.2 Realtime software

The control algorithm is coded in MATLAB and SIMULINK®. After simulations using a mathematical dynamic model of the vessel is successful, the mathematical model is replaced by serial communication blocks for the SSC and UDP communication blocks for the sensor unit. Then the control algorithm is compiled into machine code using the xPC Target™ Embedded Option of MATLAB. The compiled code runs in realtime on the PC/104 computer on top of the xPC Target™ realtime kernel.

3 Dynamic model and parameter identification

In this section, the dynamic model of a surface vessel is derived and its parameters are identified.

3.1 Dynamic model

For the derivation of the dynamic model the vessel is assumed to be constrained by three degrees of freedom, surge, sway, and yaw. The terms u, v, and r denote the surge, sway and yaw speeds, respectively in local coordinates (SNAME

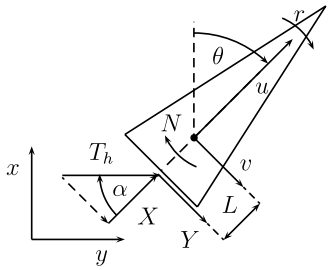

Fig. 2 A 3 DOF dynamic model of a surface vessel

1950) (Fig. 2). Under the assumptions of constant inertia, and simplification of the hydrodynamics, the dynamics of a surface vessel with an elliptical vehicle body can be described by the following equation (Fossen 1994)

$$\dot{\mathbf{q}}_l = \mathbf{m}^{-1}(\mathbf{A}(\mathbf{q}_l)\mathbf{q}_l + \mathbf{w}_l + \boldsymbol{\tau}). \tag{3}$$

$\mathbf{m}$ is a diagonal mass matrix, $\mathbf{A}$ includes Coriolis and damping term, and $\mathbf{w} = [w_u, w_v, w_r]^T$ is the disturbance force. The term $\boldsymbol{\tau} = [X, Y, N]^T$ refers to the driving force of the surface vessel, whose components are shown in Fig. 2.

To obtain the dynamic equation in terms of global coordinates $\mathbf{q}_g = [x, y, \theta]^{\mathrm{T}}$ the vector $\dot{\mathbf{q}}_l$ has to be expressed in global coordinates

$$\dot{\mathbf{q}}_l = \frac{d}{dt}(\mathbf{R}_z(\theta)\dot{\mathbf{q}}_g) = \dot{\mathbf{R}}_z(\theta)\dot{\mathbf{q}}_g + \mathbf{R}_z(\theta)\ddot{\mathbf{q}}_g, \tag{4}$$

where $\mathbf{R}_z(\theta)$ is the rotation matrix about the z-axis with θ. Equating (3) and (4) and substituting $\dot{\mathbf{q}}_g$ by using $\dot{\mathbf{q}}_g = \mathbf{R}_z^{-1}(\theta)\mathbf{q}_l$ allows the calculation of $\ddot{\mathbf{q}}_g = f(\dot{\mathbf{q}}_g, n, \alpha)$

$$\ddot{\mathbf{q}}_g = \mathbf{R}_z^{-1}(\theta)[\mathbf{m}^{-1}(\mathbf{A}\mathbf{q}_l + \mathbf{w}_l + \mathbf{d}) - \dot{\mathbf{R}}_z(\theta)\mathbf{R}_z^{-1}(\theta)\mathbf{q}_l]. \tag{5}$$

In a next step, the model of the propellers is derived in order to find a between (n, α), and (X, Y, N). The surface vessel used for the tests has two parallel fixed blade propellers with a controllable angular speed of revolutions n and a controllable angle α. A schematic draft of the propeller configuration is shown in Fig. 3. The two propellers have different rotational directions in order to cancel out the roll moment. The two propellers are generating a total thrust of T_h which can be calculated, under the assumption that the ratio between the speed of the water going into the propeller and the drive engine speed is constant during operations (Fossen 1994) with

$$T_h = 2\rho D^4 K_T |n| n, \tag{6}$$

where ρ is the water density, D the diameter of the thruster, and K_T a design dependent thrust coefficient. The driving forces and moments can be derived (Figs. 2 and 3)

Fig. 3 Propeller configuration

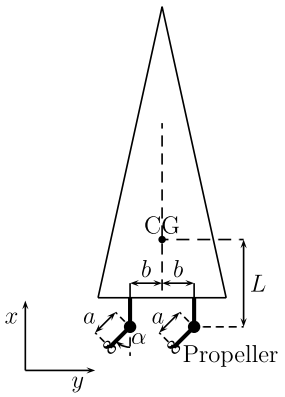

$$X = T_h \cos\alpha, \tag{7}$$

$$Y = T_h \sin\alpha, \tag{8}$$

$$N = -T_h L \sin\alpha. \tag{9}$$

These driving forces and torque will be determined by the controller. Then, the physical control inputs $[n, \alpha]$ can be calculated as

$$n = \mathrm{sign}(X)[\sqrt[4]{X^2 + Y^2}/\sqrt{2\rho D^4 K_t}], \tag{10}$$

$$\alpha = \arctan(Y/X). \tag{11}$$

3.2 Parameter identification

The dynamic equation of motion (3) of the vessel includes seven nominal parameters: three masses $\widehat{m}_{11}$, $\widehat{m}_{22}$, and $\widehat{m}_{33}$; three damping coefficients $\widehat{d}_{11}$, $\widehat{d}_{22}$, and $\widehat{d}_{33}$; and a thrust coefficient $\widehat{K}_t$. All the equations of motion can be divided by $\widehat{m}_{11}$ without affecting the dynamic model. This means that six new parameters can be defined as ratios of all other parameters to m_{11}, which reduces the number of parameters for identification. Or equivalently, $\widehat{m}_{11}$ can be specified without loss of generality, and the other six parameters can be identified. Here, $\widehat{m}_{11}$ is assumed to be equal to the mass of the vessel, and a vector $\widehat{\mathbf{X}}$ is defined that contains the remaining six parameters to be identified:

$$\widehat{\mathbf{X}} = \begin{bmatrix} \widehat{m}_{22} & \widehat{m}_{33} & \widehat{d}_{11} & \widehat{d}_{22} & \widehat{d}_{33} & \widehat{K}_t \end{bmatrix}^T.$$

In order to identify the parameters open-loop tests are performed by using the surface vessel in Sect. 2. The obtained data are used to estimate the parameters with the method of least-square error of Carl Friedrich Gauss. Therefore, the dynamic model (3) is rewritten as

$$-\mathbf{m}\dot{\mathbf{q}}_l + \mathbf{A}(\mathbf{q}_l)\mathbf{q}_l + \boldsymbol{\tau} = 0, \tag{12}$$

where the wave disturbance forces are assumed to be zero. This implies that the identification tests must be done where minimum amount of disturbance exists. For calculating an

Table 1 Summary of the test vessel parameters

Masses and inertias		
$\widehat{m}_{11}$	$\widehat{m}_{22}$	$\widehat{m}_{33}$
7.8 kg	8.4 kg	0.4 kg m^2
Damping coefficients		
$\widehat{d}_{11}$	$\widehat{d}_{22}$	$\widehat{d}_{33}$
20.7 kg/s	26.5 kg/s	2.2 kg m^2/s
Miscellaneous data		
$\widehat{K}_t$		0.13
L		21 cm
ρ		998 kg/m^3
D		47 mm
Uncertainty		15%

Table 2 Summary of the test vessel's measurement and parameters' uncertainty

Measurement uncertainty	
Δu	± 0.01 m/s
Δv	± 0.01 m/s
Δr	± 0.5 deg/s
$\Delta \dot{u}$	± 0.01 m/s^2
$\Delta \dot{v}$	± 0.01 m/s^2
$\Delta \dot{r}$	± 0.5 deg/s^2
Parameter uncertainty	
$\sigma_{m_{22}}$	$\pm 4.9\%$
$\sigma_{m_{33}}$	$\pm 96.3\%$
$\sigma_{d_{11}}$	$\pm 5.9\%$
$\sigma_{d_{22}}$	$\pm 2.8\%$
$\sigma_{d_{33}}$	$\pm 4.7\%$
σ_{K_t}	$\pm 7.1\%$

estimate of the parameters according to the least square method the following equations can be used for calculating the coefficients for each parameter.

$$\frac{\partial}{\partial \widehat{X}_j} \frac{1}{2} \sum_{k=0}^{N} \| - \mathbf{m}\dot{\mathbf{q}}_{l_k} + \mathbf{A}\mathbf{q}_{l_k} + \mathbf{u}_k \|_2 = 0, \quad j = 1, \ldots, 6, \tag{13}$$

where N is the number of points at which the states are sampled during the open-loop tests. These equations can be rearranged to

$$\widehat{\mathbf{X}} = \mathbf{Q}^{-1}\mathbf{B}. \tag{14}$$

At least two sets of independent measurement data u_k, v_k, r_k, $\dot{u}_k$, $\dot{v}_k$, and $\dot{r}_k$ and thrust terms X'_k and Y'_k with $k = 1, 2$ are required to calculate one set of vessel parameters, i.e., $N \geq 2$. Further, all disturbances $\mathbf{w}_l$ for the parameter identification are neglected. All parameter identifications were performed outdoors in a pond with minimum disturbance. The tests were performed with different fixed rudder angles α. The engine speed n is ramped up from zero, held constant, and then ramped down to zero. Table 1 summarizes the estimated parameters for the test boat used for tests of the controller.

A sensitivity analysis is performed to be able to estimate the uncertainty of the nominal parameters due to the measurement error of the vessel's motion. Here, the uncertainty is estimated with finite differences because a closed analytical approach such as the calculation of the total derivative (Bronstein and Semendyayev 1985) would involve the symbolical solution of (14), which would result in a very complex solution. The finite differences are given with

$$\Delta \widehat{\mathbf{X}} \geq \max |\widehat{\mathbf{X}} - \widehat{\mathbf{X}}'|, \tag{15}$$

where $\widehat{\mathbf{X}}$ and $\widehat{\mathbf{X}}'$ are calculated using the actual measured states (e.g. u) and the bounds of uncertainty for the measured states (e.g. $u \pm \Delta u$), respectively. The "max" function works on individual components of $|\widehat{\mathbf{X}} - \widehat{\mathbf{X}}'|$. The measurement and parameter uncertainties are summarized in Table 2, in which, for example, $\sigma_{m_{22}} = \pm \Delta \widehat{X}_1 / \widehat{X}_1$. Note that X_1 is the first element of $\widehat{\mathbf{X}}$.

4 Zero-dynamics stability

The vessel is controlled by using the concept of the control point. As the surface vessel is underactuated, only two of the three degrees of freedom can be directly controlled. Therefore, the position $[x_p, y_p]$ of the control point p with respect to the leaders will be controlled (Fig. 4) as the heading angle θ of the vessel is not the main concern. After the formation has reached its steady-state, the control point p of the follower remains at a fixed position with respect to the leader vessel during the motion of the formation. However, the follower vessel may oscillate about the control point p during the formation maneuvers, and this oscillation is referred to as zero-dynamics, because the yaw-angle of the underactuated vessel is not directly controlled. The yaw motion could result in an oscillatory trajectory for the center of gravity (CG) of the follower. However, as the oscillation would be about the control point p, which is attached to the follower vessel, the vessel's degrees of freedom are not independent. Therefore, it is sufficient to investigate the stability of only one of the DOFs. This is consistent with the fact that the vessel has only one unactuated DOF.

The configuration variable for the zero-dynamics stability can be selected arbitrarily. However, choosing a representative of the orientation of the follower is more intuitive and results in a simpler formulation. To investigate the zero-dynamics of this orientation, the configuration shown

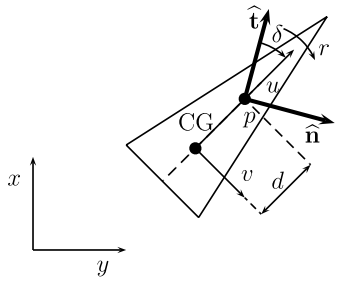

Fig. 4 Velocity of point p, which is along $\hat{\mathbf{t}}$, makes an angle δ with the orientation of the follower (modified after Fahimi 2007a)

in Fig. 4 is assumed. The velocity and acceleration of point p is known as the vessel follows the leader(s) with some prescribed offset. The angle between the inertial velocity of point p and the vessel's orientation is denoted as δ (Fig. 4). If this difference is asymptotically stable for different types of motion of point p, then the zero-dynamics of the follower is stable. Let us assume a general planar motion for the control point p with linear velocity u_p, linear acceleration $\dot{u}_p$ and radius of curvature ρ (Fahimi et al. 2008). The unit vectors tangent and perpendicular to the path of the control point p, are $\hat{\mathbf{t}}$ and $\hat{\mathbf{n}}$, respectively (Fig. 4). Therefore, the velocity and acceleration vectors of point p can be expressed as

$$\mathbf{v}_{p,(\hat{\mathbf{t}},\hat{\mathbf{n}})} = \begin{bmatrix} u_p & 0 \end{bmatrix}^T, \tag{16}$$

$$\mathbf{a}_{p,(\hat{\mathbf{t}},\hat{\mathbf{n}})} = \begin{bmatrix} \dot{u}_p & \dfrac{u_p^2}{\rho} \end{bmatrix}^T, \tag{17}$$

where ρ is the radius of curvature of the control point's path. The velocity and acceleration of the center of gravity can be expressed as $\mathbf{v}_{\mathrm{CG},(\hat{\mathbf{t}},\hat{\mathbf{n}})} = f(\mathbf{v}_{p,(\hat{\mathbf{t}},\hat{\mathbf{n}})})$, and $\mathbf{a}_{\mathrm{CG},(\hat{\mathbf{t}},\hat{\mathbf{n}})} = f(\mathbf{a}_{p,(\hat{\mathbf{t}},\hat{\mathbf{n}})})$, respectively. Substituting these functions into the second and third dynamic equation (3), noting that

$$r = \dot{\delta} + \frac{u_p}{\rho}, \qquad \dot{r} = \ddot{\delta} + \frac{\dot{u}_p}{\rho}, \tag{18}$$

and linearizing around $\delta = 0$ yields:

$$a\ddot{\delta} + b\dot{\delta} + e\delta = f. \tag{19}$$

Next, stability for the operational conditions considered in the subsequent sections is examined.

4.1 Stability for curvilinear motions with constant speed

In the case of curvilinear motions with constant speed, $u_p = \overline{u}_p$ and $\dot{u}_p = 0$ indicate the constant speed of the motion. Applying this assumption to (19) yields the characteristic equation

$$ap^2 + bp + e = 0, \tag{20}$$

where

$$a = [m_{33} - m_{22}Ld]/m_{11},$$
$$b = [(m_{11}(L-d) + m_{22}d)\overline{u}_p - d_{22}Ld + d_{33}]/m_{11},$$
$$c = [-d_{22}\overline{u}_p L + (m_{22} - m_{11})\overline{u}_p^2]/m_{11}.$$

The stability of the follower can be investigated by computing the roots

$$p_{1,2} = -\frac{1}{2a}[b \pm \sqrt{b^2 - 4ac}]. \tag{21}$$

The roots of the characteristic (20) must be either negative real numbers or complex conjugates with negative real parts in order to ensure a stable behavior. Even a general analysis of this simplified equation is a very elaborate task. Therefore, a numerical approach is used. Ratios typical for vessels scaled by m_{11} are utilized for this analysis. These ratios were obtained from the parameter identification (see Sect. 3.2).

$$\frac{m_{22}}{m_{11}} = 1.08, \qquad \frac{m_{33}}{m_{11}} = 0.05 \text{ m}^2,$$
$$\frac{d_{22}}{m_{11}} = 3.40 \text{ s}^{-1}, \qquad \frac{d_{33}}{m_{11}} = 0.30 \text{ m}^2/\text{s}, \qquad L = 0.21 \text{ m}.$$

Further, a dimensionless parameter is defined as $\kappa = d/L$ to represent the distance d between the control point p and CG of the vessel (Fig. 4). These assumptions yield

$$a = [0.05 - 4.8 \cdot 10^{-2}\kappa] \text{ m}^2,$$
$$b = [(0.21 + 1.7 \cdot 10^{-2}\kappa)\overline{u}_p - 0.15\kappa + 0.30] \text{ m}^2/\text{s},$$
$$c = [-0.71\overline{u}_p + 0.08\overline{u}_p^2] \text{ m}^2/\text{s}^2.$$

(Note that $\overline{u}_p$ has to be in [m/s].)

The root plots for two scenarios are shown in Figs. 5 and 6. First, a constant forward speed of $\overline{u}_p = 0.5$ m/s was assumed, and the roots were investigated for different values of $\kappa = \frac{d}{L} = 0, \ldots, 20$. This investigation shows that the second-order zero-dynamics of the system has an overdamped response when $\kappa > 7.4$, has a critically damped response when $\kappa \approx 7.4$, and has an underdamped response when $2.9 < \kappa < 7.4$. For ratios $\kappa \leq 2.9$, the zero-dynamics is unstable.

Second, a ratio $\kappa = d/L = 9.5$ (overdamped system behavior) is chosen because oscillatory motions of the vessel are highly undesirable. For this ratio, different constant forward speeds $\overline{u}_p = 0, \ldots, 20$ m/s are chosen, and the roots are calculated. This investigation shows that the second-order zero-dynamics of the system has an overdamped response when $\overline{u}_p < 0.7$ m/s, has a critically damped response when $\overline{u}_p \approx 0.7$ m/s, and has an underdamped response when $0.7 \text{ m/s} < \overline{u}_p < 3.0$ m/s. For velocities $\overline{u}_p \geq 3.0$ m/s, the zero-dynamics is unstable. The experimental vessel tested is able to achieve a maximal velocity of only

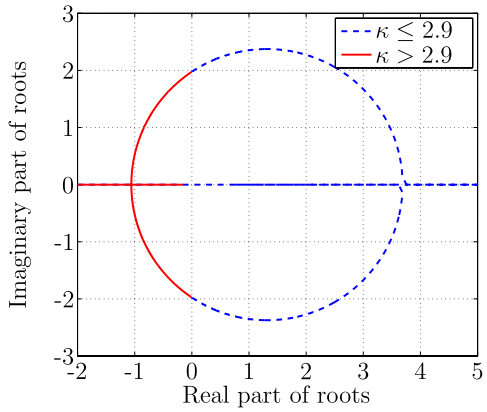

Fig. 5 Root plot of characteristic equation with a constant forward speed $\overline{u}_p = 0.5$ m/s and different values of $\kappa = d/L$

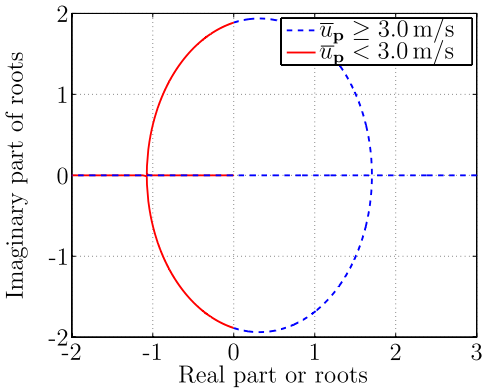

Fig. 6 Root plot of characteristic equation with a constant $\kappa = d/L = 9.5$ and a different constant forward speed $\overline{u}_p$

1.0 m/s, so it cannot reach the unstable bound of the velocity.

4.2 Equilibrium orientation for circular and linear motions with constant speed

Determining the equilibrium point of the orientation of the follower vessel for practical motions is essential. Here, this equilibrium orientation is derived for the circular motion of the leaders. For the circular motion with constant speed, $u_p = \overline{u}_p$, and $\dot{u}_p = 0$. At the equilibrium orientation, δ^e, the derivatives $\ddot{\delta}$ and $\dot{\delta}$ are zero. Applying these assumptions to the linearized (19) results in

$$\delta^e = \frac{ae}{c}, \tag{22}$$

where

$$e = \frac{(d_{33} - d_{22}Ld)\overline{u}_p - [(L+d)m_{22} + (L-d)m_{11}]\overline{u}_p^2}{(m_{33} - m_{22}Ld)\rho}.$$

Dividing the numerator and denominator by m_{11}, applying the ratios given in (22), and simplifying yield

$$\delta^e = \frac{0.3 - 0.15\kappa - 0.44 \cdot (1+\kappa)\overline{u}_p}{(0.08\overline{u}_p - 0.71)\rho}. \tag{23}$$

(Note that $\overline{u}_p$ has to be in [m/s] and ρ in [m].)

Equation (23) indicates that δ, the difference between the orientation of the follower vessel and the direction of the velocity of the control point p, converges to the constant δ^e when the control point p has a circular motion with constant speed. For a linear motion $\rho \to \infty$; therefore, (23) reduces to $\delta^e = 0$. For a linear motion, the orientation of the motion of point p as attached to the leader vessel is in fact the orientation of the leader's motion. A zero-equilibrium orientation difference means that the leader and the follower vessel in a linear motion become parallel.

5 Formation scheme

In this section, a formation scheme for arbitrary formation control is presented. The broad availability of cost efficient differential global positioning systems (DGPS), inertial measurement units (IMU), and high performance computers creates the possibility of implementing new nonlinear formation control schemes and applying them to a large number of surface vessels to create arbitrary formations or swarms. The formation control of autonomous vessels has many advantages compared to trajectory-tracking of vessels. It increases the robustness and redundancy, possibility of reconfiguration and the structure flexibility for the formation group because the proposed formation control is a decentralized approach where a number of vessels can follow one leader in a given geometrical formation.

To be able to operate arbitrary formation configurations, two leader-follower formation control schemes are needed (Desai 2002). First, formation control for configurations of two vessels has to be considered by controlling the distance and the angle between the leader vessel and the follower vessel. Second, the distance of the control point of the follower vessel to the center of gravity (CG) of two leader vessels has to be controlled. By using these two control schemes it is possible to achieve arbitrary formation configurations. The focus in this paper (controller derivation, experiments, etc.) is on the second control scheme.

5.1 l–ψ control scheme

Figure 7 shows the l–ψ formation control approach for a surface vessel. The vessels are controlled by maintaining a desired distance l_{12}^d between the control point p of the follower and the CG of the leader, and a desired relative angle ψ_{12}^d, where superscript "d" stands for "desired." The distance between the control point p and the CG of the follower is denoted as d (Desai 2002).

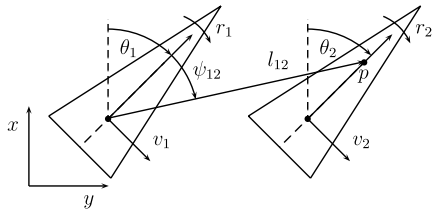

Fig. 7 l–ψ control configuration

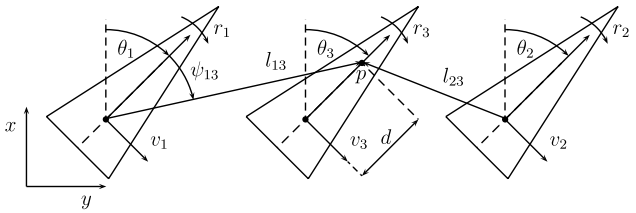

Fig. 8 l–l control configuration

5.2 l–l control scheme

Figure 8 shows the l–l formation control approach. The aim in this control approach is to maintain the desired distances, l_{13}^d and l_{23}^d, between the follower and its two leaders (Desai 2002). The objective of the controller is to stabilize the two outputs $[l_{13}, l_{23}]$ by using the two inputs $[n, \alpha]$, but the input-output equations are needed. These equations can be obtained by deriving the kinematic equations $[\ddot{l}_{13}, \ddot{l}_{23}] = f(\mathbf{q}_{g_1}, \dot{\mathbf{q}}_{g_1}, \ddot{\mathbf{q}}_{g_1}, \mathbf{q}_{g_2}, \dot{\mathbf{q}}_{g_2}, \ddot{\mathbf{q}}_{g_2}, \mathbf{q}_{g_3}, \dot{\mathbf{q}}_{g_3}, \ddot{\mathbf{q}}_{g_3})$ and substituting the term $\ddot{\mathbf{q}}_{g_3}$ by using $\ddot{\mathbf{q}}_{g_3} = f(\dot{\mathbf{q}}_{g_3}, n, \alpha)$; hence, relating the outputs to the inputs (5).

The kinematic equations $[\ddot{l}_{13}, \ddot{l}_{23}]$ can be derived by performing an acceleration analysis. This acceleration analysis yields

$$\ddot{\mathbf{l}} = \mathbf{T}\ddot{\mathbf{q}}_{g_3} + \mathbf{B}, \tag{24}$$

where

$$\ddot{\mathbf{l}} = [\ddot{l}_{13}, \ddot{l}_{23}]^T,$$

$$\mathbf{B} = -\begin{bmatrix} \ddot{x}_1 \sin\alpha_1 + \ddot{y}_1 \cos\alpha_1 \\ \ddot{x}_2 \sin\alpha_2 + \ddot{y}_2 \cos\alpha_2 \end{bmatrix} - d\dot{\theta}_3^2 \begin{bmatrix} \cos\gamma_1 \\ \cos\gamma_2 \end{bmatrix} + \begin{bmatrix} l_{13}\dot{\alpha}_1^2 \\ l_{23}\dot{\alpha}_2^2 \end{bmatrix},$$

$$\mathbf{T} = \begin{bmatrix} \cos\alpha_1 & \sin\alpha_1 & d\sin\gamma_1 \\ \cos\alpha_2 & \sin\alpha_2 & d\sin\gamma_2 \end{bmatrix}.$$

For the above equations, the angles and their derivatives can be computed as

$$\alpha_i = \theta_i + \psi_{13},$$

$$\dot{\alpha}_i = \dot{\theta}_i + \dot{\psi}_{13},$$

$$\gamma_i = \theta_i + \psi_{i3} - \theta_3.$$

Now, the term $\ddot{\mathbf{q}}_{g_3}$ in (24) can be easily substituted by using (5), which yields the input-output equation in the standard matrix form

$$\ddot{\mathbf{l}} = \mathbf{f} + \mathbf{w} + \mathbf{bu}, \tag{25}$$

where

$$\mathbf{f} = \mathbf{T}\mathbf{R}_z^{-1}(\theta_3)(\mathbf{m}^{-1}\mathbf{A} - \dot{\mathbf{R}}_z(\theta_3)\mathbf{R}_z^{-1}(\theta_3))\mathbf{q}_l + \mathbf{B},$$

$$\mathbf{w} = \mathbf{T}\mathbf{R}_z^{-1}(\theta_3)\mathbf{m}^{-1}\mathbf{w}_l,$$

$$\mathbf{bu} = \mathbf{T}\mathbf{R}_z^{-1}(\theta_3)\mathbf{m}^{-1}\mathbf{K}_t\mathbf{u},$$

$$\mathbf{K}_t = \begin{bmatrix} K_t & 0 \\ 0 & K_t \\ 0 & -LK_t \end{bmatrix},$$

and $\mathbf{u} = [X', Y']^T = \frac{1}{K_t}[X, Y]^T$ is the controller input.

5.3 Trajectory planning

Large tracking errors may occur during the formation initialization. These tracking errors may cause the controller to request very large inputs $[n, \alpha]$. However, due to the mechanical limitations of the vessel, the vessel's actuators may not be able to realize these inputs. This actuator saturation may cause an instability of the vessel. To solve this problem, an output trajectory planning is introduced that manipulates the desired outputs $[l_{13}^d(t), l_{23}^d(t)]$ such that these desired values are initially close to the current outputs $[l_{13}^{t_0}, l_{23}^{t_0}]$ at control initialization and so that

$$\lim_{t\to\infty} [l_{13}^d(t), l_{23}^d(t)]^T \to [l_{13}^d, l_{23}^d]^T, \tag{26}$$

where l_{13}^d and l_{23}^d are the final desired formation parameters.

Keeping the relative acceleration between the vessels, represented by $\ddot{l}_{13}$ and $\ddot{l}_{23}$, as small as possible is desirable. A high relative acceleration results in a very high engine speed n and, if a change of direction is involved, in a large angle α that may exceed the system limits. Therefore, it is recommended to keep the relative acceleration between the vessels $\ddot{l}_{13}$ and $\ddot{l}_{23}$ as small as possible. Figure 9 illustrates the form of a function for $l_{13}^d(t)$ and $l_{23}^d(t)$ versus time. At the time $t_{i0} = 0$ and at the time t_{i1} when the vessel reaches its desired position both the first and second derivatives (relative velocity $[\dot{l}_{13}, \dot{l}_{13}]$ and relative acceleration $[\ddot{l}_{13}, \ddot{l}_{13}]$ between the vessels) are set to zero.

This function can be obtained by interpolation with the following equation, giving the desired output trajectory

$$\begin{bmatrix} l_{i3}^d(t) \\ \dot{l}_{i3}^d(t) \\ \ddot{l}_{i3}^d(t) \end{bmatrix}$$

$$= \begin{bmatrix} t^5 & t^4 & t^3 & t^2 & t & 1 \\ 5t^4 & 4t^3 & 3t^2 & 2t & 1 & 0 \\ 20t^3 & 12t^2 & 6t & 2 & 0 & 0 \end{bmatrix} \begin{bmatrix} a_{i1} \\ a_{i2} \\ a_{i3} \\ a_{i4} \\ a_{i5} \\ a_{i6} \end{bmatrix}, \quad (27)$$

where

$$\begin{bmatrix} a_{i1} \\ a_{i2} \\ a_{i3} \\ a_{i4} \\ a_{i5} \\ a_{i5} \end{bmatrix} = \begin{bmatrix} t_{i0}^5 & t_{i0}^4 & t_{i0}^3 & t_{i0}^2 & t_{i0} & 1 \\ 5t_{i0}^4 & 4t_{i0}^3 & 3t_{i0}^2 & 2t_{i0} & 1 & 0 \\ 20t_{i0}^3 & 12t_{i0}^2 & 6t_{i0} & 2 & 0 & 0 \\ t_{i1}^5 & t_{i1}^4 & t_{i1}^3 & t_{i1}^2 & t_{i1} & 1 \\ 5t_{i1}^4 & 4t_{i1}^3 & 3t_{i1}^2 & 2t_{i1} & 1 & 0 \\ 20t_{i1}^3 & 12t_{i1}^2 & 6t_{i1} & 2 & 0 & 0 \end{bmatrix}^{-1} \begin{bmatrix} l_{i3}^{t_0} \\ 0 \\ 0 \\ l_{i3}^{d} \\ 0 \\ 0 \end{bmatrix}.$$

Note that a fifth order curve has been used to have control over the first and second derivative of the parameters. The first and second derivative of the outputs vanish at the start and the end of the trajectory, leading to a very smooth transition between the two states. The time t_{i0} indicates the time of the trajectory planning reset (usually 0), and $t_{i1} - t_{i0}$ is the time to approach l_{i3}^d. The value for t_{i1} is constrained such that the relative velocity between the two vehicles $\dot{l}_{i3}$ is not larger than a threshold ξ. This t_{i1} is calculated by solving the following equation

$$[\mathbf{T}(0, 0.5t_{i1})^{-1} \cdot \mathbf{l}_{\mathbf{i3}}^*]^T [5t_{i1}^4, 4t_{i1}^3, 3t_{i1}^2, 2t_{i1}, 1, 0]^T = \xi. \quad (28)$$

Extensive computer simulations have shown that the vessel can easily track the smooth trajectories planned by this algorithm. An example of the achieved tracking error is presented in Fig. 10, in which $E = l_{i3}^d(t) - l_{i3}^d$ and the initial error of $l_{i3}^{t_0} - l_{i3}^d = 95$ m from the final desired parameters l_{i3}^d exists and t_{i1} is set to 100 s.

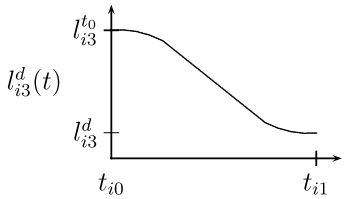

Fig. 9 Desired function for output trajectory planning

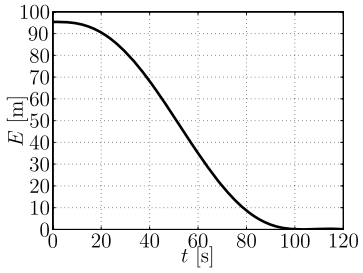

Fig. 10 Computer simulation of the tracking error E for the proposed planned tracking error approach

6 Control design

One approach to robust formation control is the Sliding Mode control methodology. This method is chosen for formation control because it allows a systematic approach to the problem of maintaining stability and consistent performance in the face of modeling imprecision. Further, it is a proven method applied to a number of applications such as robot manipulators (Tsaprounis and Aspragathos 1999), underwater vehicles (Innocenti and Campa 1999), marine crafts (Fahimi 2007a), helicopters (Fahimi 2008), automotive engines (Bhatti et al. 1999), electric motors (Proca et al. 2003) and power systems (Dash et al. 1996).

In theory, sliding mode control is able to achieve 'perfect' performance in the presence of arbitrary parameter inaccuracies. However, in practice perfect performance would result in an unfavorable high control activity for large parameter uncertainty and disturbances. This high control activity is at odds with the neglected dynamics of the vessel model. Therefore, a trade-off between tracking performance and the bound of the parametric uncertainty has to be found by tuning the sliding mode controller (Slotine and Li 1991).

A proportional-integral-derivative (PID) controller is used to initiate the vessel's angle and velocity during the start-up of the formation because the sliding-mode controller was optimized for small deviations from the desired values for the velocity and angle.

6.1 Proportional-integral-derivative controller

The PID controller was used to initialize the follower with the desired speed u^d and the desired angle θ_3^d. The desired initial angle θ_3^d is obtained by assuming that the vessel moves tangent to its motion path. The PID control laws of this so called 'course-keeping autopilot' (Fossen 1994) can be given by:

$$n|n| - n^d|n^d| = -K_{P_n}\tilde{u} - K_{D_n}\dot{\tilde{u}} - K_{I_n}\int_0^t \tilde{u}dt, \quad (29)$$

$$\alpha - \alpha^d = K_{P_\alpha}\tilde{\theta} + K_{D_\alpha}\dot{\tilde{\theta}} + K_{I_\alpha}\int_0^t \tilde{\theta}dt, \quad (30)$$

where $\tilde{u} = u - u^d$ and $\tilde{\theta} = \theta - \theta^d$. The desired values for the inputs $[n^d, \alpha^d]$ can be calculated by using

$$n^d|n^d| = \text{sign}(X^d)\frac{\sqrt{(X^d)^2 + (Y^d)^2}}{\rho D^4 K_t}, \quad (31)$$

$$\alpha^d = \arctan\left(\frac{Y^d}{X^d}\right). \quad (32)$$

Table 3 Summary of PID controller parameters

u-controller		θ-controller	
K_{P_n}	0.01 1/m s	K_{P_α}	3
K_{D_n}	0.1 1/m	K_{D_α}	0.5 s
K_{I_n}	0.05 1/m s^2	K_{I_α}	0.4 s^{-1}

The desired values for the forces X^d and Y^d can be derived from the dynamic model (3).

$$X^d = m_{11}\dot{u}^d - m_{22}vr^d + d_{11}u^d, \tag{33}$$

$$Y^d = -\frac{1}{L}(m_{33}\dot{r}^d - (m_{22} - m_{11})u^d v + d_{33}r^d). \tag{34}$$

Table 3 summarizes the used parameters. The controller gains are found by experimental tuning.

6.2 Sliding mode controller

The goal of the model-based sliding-mode formation controller is to stabilize the two outputs $[l_{13}, l_{23}]$ by using the two inputs $[n, \alpha]$. In order to derive the control law, a time-varying surface in the input-output space $\mathbf{R}^{(2)}$ is defined by two scalar equations $\mathbf{s}(\mathbf{l}; t) = 0$ (Slotine and Li 1991). (Note: Given the initial conditions $\mathbf{l}^d(0) = \mathbf{l}(0)$ the problem of tracking $\mathbf{l} = \mathbf{l}^d(t)$ is equivalent to that of remaining on the surface without loss of generality.)

$$\mathbf{s}(\mathbf{l}, t) = \left(\frac{d}{dt} + \mathbf{\Lambda}\right)(\mathbf{l} - \mathbf{l}^d) = \dot{\mathbf{l}} - \mathbf{s}_r = \mathbf{0}, \tag{35}$$

where $\mathbf{\Lambda} = \text{diagonal}_{(2\times 2)}(\lambda_1, \lambda_2)$, and $\lambda_i > 0$. The term $\mathbf{e} = (\mathbf{l} - \mathbf{l}^d)$ is the tracking error between the actual values $\mathbf{l} = [l_{13}, l_{23}]$ and the desired value $\mathbf{l}^d = [l_{13}^d, l_{23}^d]$. The term $\mathbf{s}_r$ can be written as

$$\mathbf{s}_r = \begin{bmatrix} \dot{l}_{13}^d - \lambda_1(l_{13} - l_{13}^d) \\ \dot{l}_{23}^d - \lambda_2(l_{23} - l_{23}^d) \end{bmatrix}, \tag{36}$$

where λ_i is a constant which can be described as a gain for the tracking error; a large value λ_i sets a high penalty on the deviation of the output from the desired values.

To obtain the control law (35) is differentiated and $\ddot{\mathbf{l}}$ is substituted by using (25). These manipulations yield to the equation of the so-called equivalent control $\mathbf{u}_{eq}$, which can be interpreted as the continuous control law that would keep the trajectories on the surface in the absence of unknown disturbances and if the dynamics were exactly known. (Note: The trajectories are supposed to remain on the surface, therefore the first derivative of the surface vanishes ($\dot{\mathbf{s}} = 0$).)

$$\widehat{\mathbf{b}}\mathbf{u}_{eq} = -\widehat{\mathbf{f}} - \widehat{\mathbf{w}} + \dot{\mathbf{s}}_r, \tag{37}$$

where $\widehat{\ }$ indicates that the matrices are evaluated for the nominal values of the system parameters and disturbances.

To meet the sliding condition despite the uncertainties and disturbances a discontinuous term needs to be added, which ensures that the trajectories reach the surface within a finite time. The term can be defined as

$$\widehat{\mathbf{b}}\mathbf{u} = \widehat{\mathbf{b}}\mathbf{u}_{eq} - \mathbf{K} \cdot \text{sat}(\mathbf{s}, \boldsymbol{\phi}), \tag{38}$$

where $\mathbf{K} = \text{diagonal}_{(2\times 2)}(k_1, k_2)$ is the controller's nonlinearity gain and depends on the uncertainty. Finally, (37) and (38) yield to the controller

$$\mathbf{u} = \widehat{\mathbf{b}}^{-1}(-\widehat{\mathbf{f}} - \widehat{\mathbf{w}} + \dot{\mathbf{s}}_r - \mathbf{K} \cdot \text{sat}(\mathbf{s}, \boldsymbol{\phi})). \tag{39}$$

The function

$$\text{sat}(s_i, \phi_i) = \begin{cases} \frac{s_i}{\phi_i}, & |s_i| \le \phi_i \\ \text{sign}(s_i), & |s_i| > \phi_i \end{cases} \tag{40}$$

is introduced to smooth out the control discontinuity around zero in order to reduce undesired chattering caused by imperfections of the switching of the discontinuous term (e.g., the switching is not instantaneous and the value of $\mathbf{s}$ is not known with infinite precision). The parameter ϕ of the 'sat' function determines the boundary layer thickness, i.e., a large value for ϕ (e.g., values greater than 1) prevents chattering but increases the tracking error, whereas small values increase chattering and decrease the tracking error. The goal is to achieve a good trade-off between tracking performance and input chattering.

The parameter $\mathbf{k}$ has to be chosen such that the system is asymptotically stable in the sense of Lyapunov to ensure safe and reliable operations at all times. To achieve this behavior, a Lyapunov function is defined

$$V(\mathbf{s}) = \frac{1}{2}\mathbf{s}^2 \ge 0. \tag{41}$$

Now the parameter $\mathbf{k}$ has to be chosen such that

$$\dot{V}(\mathbf{s}) = \frac{1}{2}\frac{d}{dt}\mathbf{s}^2 = \dot{\mathbf{s}} \cdot \mathbf{s} \le -\boldsymbol{\eta}|\mathbf{s}|, \tag{42}$$

where $\boldsymbol{\eta} = [\eta_1, \eta_2]$ are strictly positive constants, which can be used for the controller setting. For a controller, which should respond to set point changes, $\boldsymbol{\eta}$ has to be chosen fairly small to prevent very large input values. If the controller meets the requirements of (42) the system is asymptotically stable in the sense of Lyapunov. If $\dot{\mathbf{s}} \cdot \mathbf{s} > -\boldsymbol{\eta}|\mathbf{s}|$ during the operation, the operator of the system should be alerted that the system is close to becoming unstable.

To calculate $\mathbf{k}$, the term $\dot{\mathbf{s}}$ can be derived from the first differentiation of (35)

$$\mathbf{s}(\mathbf{l}; t) = \dot{\mathbf{l}} - \dot{\mathbf{l}}^d + \mathbf{\Lambda}(\mathbf{l} - \mathbf{l}^d). \tag{43}$$

After differentiating and substituting $\ddot{\mathbf{l}}$ from (25), one can show that

$$\dot{\mathbf{s}}(\mathbf{l}; t) = \mathbf{f} + \mathbf{w} + \mathbf{b}\mathbf{u} - \ddot{\mathbf{l}}^d + \mathbf{\Lambda}(\dot{\mathbf{l}} - \dot{\mathbf{l}}^d). \tag{44}$$

Now, the term $\mathbf{u}$ can be substituted by using (39). Finally, substituting $\mathbf{s}$ and $\dot{\mathbf{s}}$ into (42), rearranging, and simplifying yields to a lower bound for $\mathbf{k} = [k_1, k_2]^T$

$$\mathbf{k} \geq \widehat{\mathbf{b}}\widehat{\mathbf{b}}^{-1}[|\mathbf{f} - \widehat{\mathbf{f}}| + |\mathbf{w} - \widehat{\mathbf{w}}| + |(1 - \mathbf{b}\widehat{\mathbf{b}}^{-1})(\dot{\mathbf{s}}_\mathbf{r} - \widehat{\mathbf{f}} - \widehat{\mathbf{w}})| + \boldsymbol{\eta}]. \tag{45}$$

The terms $\mathbf{f}$ and $\mathbf{b}$ can be calculated by estimating an upper bound for the actual parameter values $\mathbf{X} = [m_{22}, \ldots, d_{33}, K_t]^T$. This bound can be found by adding the estimated maximum uncertainties of the parameter identification $[\sigma_{m_{22}}, \ldots, \sigma_{d_{33}}, \sigma_{K_t}]$ (Table 2) to the nominal values $\widehat{\mathbf{X}} = [\widehat{m}_{22}, \ldots, \widehat{d}_{33}, \widehat{K}_t]^T$.

$$\mathbf{X} = [(1 + \sigma_{m_{22}})\widehat{m}_{22}, \ldots, (1 + \sigma_{k_t})\widehat{K}_t]^T. \tag{46}$$

After doing so, the terms $\widehat{\mathbf{f}}$ and $\widehat{\mathbf{b}}$, and $\mathbf{f}$ and $\mathbf{b}$ can be calculated by using (25) with $\widehat{\mathbf{X}}$ and $\mathbf{X}$, respectively. The term $|\mathbf{w} - \widehat{\mathbf{w}}|$ can be calculated by setting for $\widehat{\mathbf{w}}$ the nominal disturbance (usually zero) and for $\mathbf{w}$ the maximum allowable disturbance during operations. $\mathbf{w}$ is calculated as

$$\mathbf{w} = \mathbf{R}_z^{-1}(\theta)\mathbf{w}_l, \tag{47}$$

where $\mathbf{w}_l$ is the maximum allowable disturbance at which the vessel can be operated, expressed in the vessel's local coordinate system.

The controller matrix $\widehat{\mathbf{b}}$ has to be invertible, i.e., non-singular at all times during operation. Singularities can be found by calculating the roots of the determinant of the matrix $\widehat{\mathbf{b}}$ by computing

$$\det(\widehat{\mathbf{b}}) = \frac{(\widehat{m}_{33} - d \cdot L\widehat{m}_{22})}{\widehat{m}_{11}\widehat{m}_{22}\widehat{m}_{33}} \sin(\alpha_1 - \alpha_2) = 0. \tag{48}$$

This equation indicates that the value d has to be chosen carefully to avoid the root $d = \frac{\widehat{m}_{33}}{L\widehat{m}_{22}} = 0.23$ m. Further, the closed-loop system becomes unstable if the origin of the coordinate systems of the two leader vessels steering ($\theta_1 = \theta_2$) in the same direction and the control point of vessel 3 are collinear, i.e., $\theta_1 + \psi_{13} = (\theta_2 + \psi_{23}) + k\pi$, where $k = 1, 2, \ldots$, which has to be avoided when configuring the formation.

7 Experiments

First, the controller gains must be determined starting with initial values found by using computer simulations. Due to the mismatch between the dynamic parameters of the mathematical model and the actual test vessel, the controller gains need to be fine tuned. All parameters are improved through several closed-loop control experiments using the test vessel. The most important parameter for fine tuning the controller is $\boldsymbol{\eta}$ (42). In order to find a controller gain $\boldsymbol{\eta}$ that results in a good tracking performance of the controlled vessel various tests with different $\boldsymbol{\eta}$ values are performed, starting with low gains. Table 4 summarizes the used controller gains and parameters for the controller setting.

Table 4 Summary of the controller parameters used for the controller test

Controller Setting	$\boldsymbol{\eta}$	1.4 m/s^2
Chattering Parameter	ϕ	0.2
Distance CG-p	d	2 m
Weighting Factor	λ	0.2 1/s
Maximal allowed Disturbance	$\mathbf{w}_l$	$[3.5, 3.5, 0]^T$ N

The following sections present the experimental test results for a straight line test, a circular motion test, and a zig-zag maneuver. All tests were performed in the presence of parameter uncertainty, model uncertainty, and environmental disturbances on a very large freshwater lake (Okanagan Lake in British Columbia near Vernon).

7.1 Straight line

This subsection presents the results of a test showing the performance of the controller for a straight line motion. In the first 30 seconds of the test, the follower vessel is controlled by the PID controller, which is set to bring the vessel's speed and orientation in tune with that of the leaders. Then, the position of all the vessels are reset to their initial conditions, and the controller switches to the sliding mode algorithm to keep the follower vessel in formation with the leaders. The leaders 1 and 2 were simulated by computing

$$\begin{bmatrix} x_{1,2} \\ y_{1,2} \\ \theta_{1,2} \\ u_{1,2} \\ v_{1,2} \\ r_{1,2} \end{bmatrix} = \begin{bmatrix} 3.5 + ut \\ \pm 0.75 \\ 0 \\ (1 - e^{-\frac{t}{5}})(0.5 - u_3^{(0)}) + u_3^{(0)} \\ 0 \\ 0 \end{bmatrix}, \tag{49}$$

where $u_3^{(0)}$ is the realtime speed of the follower when switching from PID to sliding mode control. The simulation of the leaders implies that they are not exposed to any disturbance; i.e., the leader's motion is tangent to their motion path at any time, and they do not have any lateral speed component; i.e., $v = 0$.

The trajectory of the leader-follower formation is presented in Fig. 11. In the first 30 s of the test, the proportional-integral-derivative (PID) controller maintains only the forward speed u_3 and the heading θ_3. After 30 s, the positions of the leaders and the follower are reset to their initial conditions, and the vessel was controlled by the sliding mode controller. The path of the vessel under PID control is plotted using the CG, while the path of the vessel under sliding mode control is plotted for the control point. The distance between

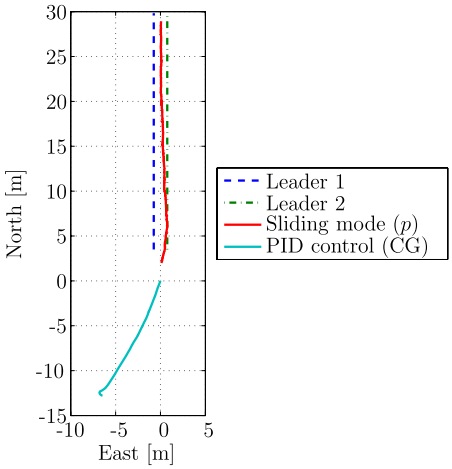

Fig. 11 Straight line: trajectory

the CG and the control point is selected as 2 m, which explains the gap between the two paths. The estimated desired angle $\theta_3^d = 0$ for the PID controller is obtained by assuming that the vessel moved tangently to its motion path. In this test, the PID controller successfully brought the vessel to an angle of approximately 0 deg, which corresponded to the angle of the virtual leaders that are not exposed to the disturbances. The disturbances, a combination of wind and waves out of West, caused the follower to perform a lateral speed component of approximately 0.2 m/s. The PID controller maintained the heading angle and the forward speed. As the vessel has three degrees of freedom but only two independent actuators, it is not possible for the PID controller to control all degrees of freedom. In this case, the lateral speed component remained unactuated; therefore, the PID controller does not counteract against the disturbances out of West, and the vessel drifts sideways (Fig. 11). However, the sliding mode controller, which controls the position of the vessel's control point with respect to the leaders, successfully counteracts the disturbances and keeps the vessel in the formation despite of the disturbances out of West.

Figure 12 presents the desired and the actual output values for l_{13} and l_{23} during the test. Even in the presence of very strong disturbances the vessel followed the leaders in a reliable manner. Figure 13 presents the inputs $[n, \alpha]$. This test was performed with a very low value for the chattering parameter; i.e., $\phi = 0.1$. Therefore, chattering was present. If chattering is undesired, one can increase the chattering parameter ϕ, e.g., to $\phi = 0.3$. However, a higher value for ϕ decreases the performance of the sliding mode controller.

Figure 14 presents the state $[x, y, \theta, u, v, r]^T$ of the CG of the follower, where x (North) and y (East) correspond to the position. Figure 14(a) shows the movement towards North, as the vessel moved with a constant forward speed the movement is as expected. The offset of the CG towards East occurred due to heavy disturbances of Eastward wind,

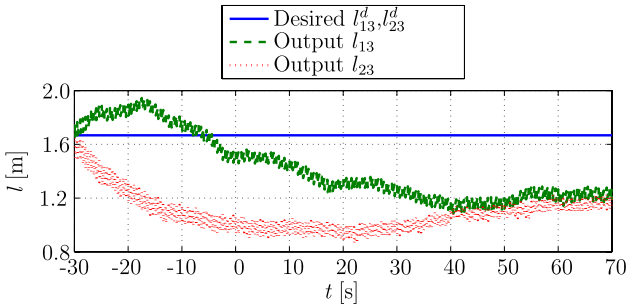

Fig. 12 Straight line: comparison of the desired values l_{13}^d and l_{23}^d and the actual outputs l_{13} and l_{23}

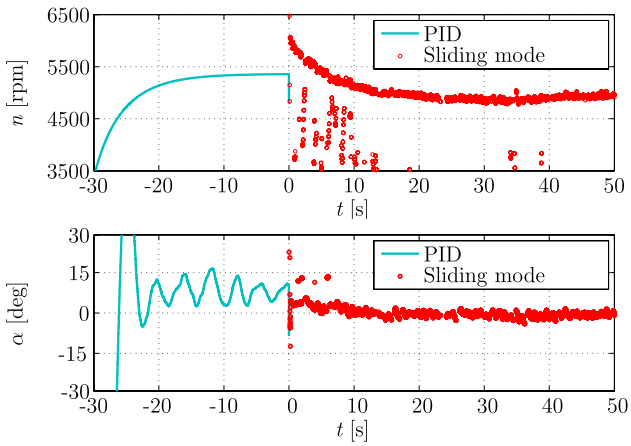

Fig. 13 Straight line: inputs $[n, \alpha]$

waves, and current (Fig. 14b). As expected it reached a steady state. However, the position of the control point p (almost) obtains its desired position. The difference between the CG and the control point p occurred because the vessel's yaw angle was not controlled and therefore not necessarily tangent to the vessel's motion path. The principals of the movement of the vessel controlled by using the concept of the control point is shown in Fig. 15. Figure 14(c) reveals also the disturbances towards East because the test vessel had to take an angle θ_3 of approximately -17 deg in order to resist the environmental disturbances. The magnitude of the vessel's speed, $\sqrt{u^2 + v^2}$, reached after a short time the same velocity as the leaders (0.5 m/s, Figs. 14d and e, and 16). As expected the angular speed about the yaw was around zero after reaching the steady state because the vessel moved in a straight line (Fig. 14f).

During this test, high disturbances, which are a combination of wave and wind out of West, are acting on the follower vessel. The total disturbance force can be estimated by using the second dynamic equation (3). When controlled by the PID controller, the vessel obtains a steady-state motion with constant speed; i.e., $\dot{v} \approx 0$ and $r \approx 0$. Further, at the steady-state motion under PID control, Fig. 13 shows $n = 5400$ rpm, and $\alpha = 6$ deg, and Fig. 14(e) reveals

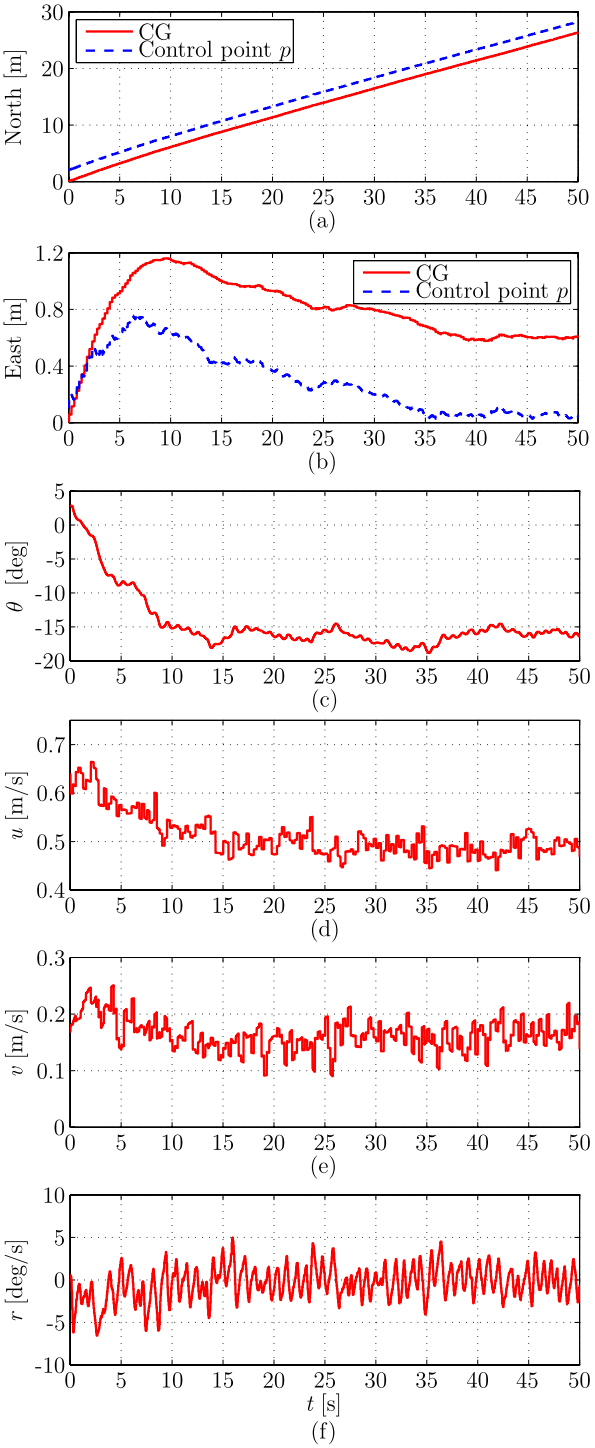

Fig. 14 Straight line: state of the center of gravity (sliding mode controlled)

$v = 0.2$ m/s at the time $t = 0$. Therefore, the total disturbance force w can be estimated by

$$w \approx w_v = d_{22}v - Y$$
$$= d_{22}v - 2\rho D^4 K_t n|n| \sin\alpha = 4.2 \text{ N}, \quad (50)$$

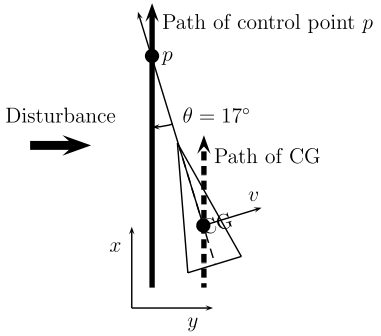

Fig. 15 A surface vessel controlled by sliding mode formation controller with high disturbances from port

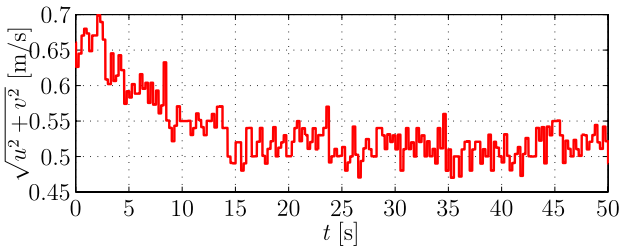

Fig. 16 Straight line: resulting speed $\sqrt{u^2 + v^2}$

which represents 21% of the maximal driving force of approximately 20 N.

7.2 Circular motion

The results of a test showing the performance of the sliding mode controller for a circular motion is presented in this section. This test is performed in rough waters in the presence of random high waves and wind gusts out of West. The disturbances can be estimated while the vessel achieves a steady-state motion under the PID control. During the PID initialization accelerations vanish: $\dot{v} \approx 0$, and $r \approx 0$. Further, at the steady-state, Fig. 18 shows $n = 5800$ rpm, and $\alpha = 8$ deg, and Fig. 20(e) reveals $v = 0.4$ m/s at the time $t = 0$. Therefore, by using the second dynamic equation (3), the total disturbances can be estimated as

$$w \approx w_v = d_{22}v - Y$$
$$= d_{22}v - 2\rho D^4 K_t n|n| \sin\alpha = 9.0 \text{ N}, \quad (51)$$

which represents 45% of the maximal driving force of approximately 20 N. The leader's motion was tangent to their motion path at any time, and they did not have any local lateral velocity; i.e., $v = 0$. The state for the circular motion

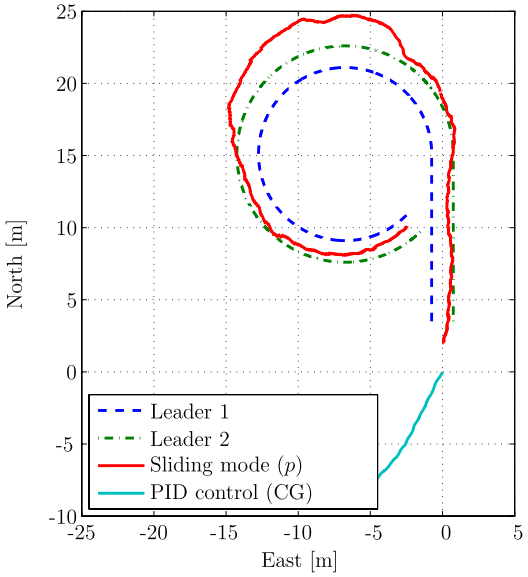

Fig. 17 Circular motion: trajectory

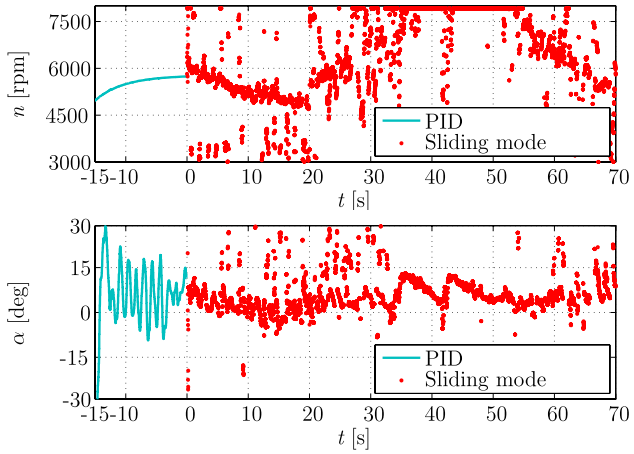

Fig. 18 Circular motion: inputs $[n, \alpha]$

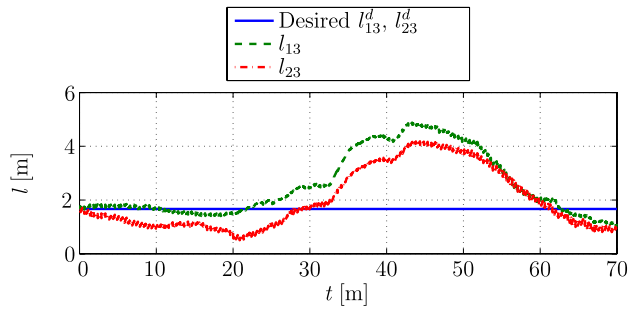

Fig. 19 Circular motion: comparison of the desired values l_{13}^d and l_{23}^d and the actual outputs l_{13} and l_{23}

could be computed by (see Sect. 7.1 for the straight line section)

$$\begin{bmatrix} x_{1,2} \\ y_{1,2} \\ \theta_{1,2} \\ u_{1,2} \\ v_{1,2} \\ r_{1,2} \end{bmatrix} = \begin{bmatrix} r_{1,2}\cos\theta_r + 12.2 \\ r_{1,2}\sin\theta_r - r_{1,2} \pm 0.75 \\ \theta_r - \frac{\pi}{2} \\ -\dot{\theta}_r r_{1,2} \\ 0 \\ \dot{\theta}_r \end{bmatrix}, \tag{52}$$

where

$$r_1 = 6 \text{ m}, \quad r_2 = 7.5 \text{ m}$$

$$\theta_r = -0.1 \text{ s}^{-1}(t - t_{\text{straight line}}) + \frac{\pi}{2},$$

$$\dot{\theta}_r = -0.1 \text{ rad/s}.$$

Figure 17 shows the path of the vessels. After a 15-second PID control interval, the sliding mode controller is activated. It can control the follower to track the desired formation on the straight-line portion and on the second half of the circular portion of the motion. However, for the first 180 deg of the circular motion, the performance is poor. In that section of the path, the vessel is not able to keep up with the leaders, because the maximum driving force of 20 N minus the 9 N Eastward disturbance force is not sufficient for the vessel to reach a global velocity equal to that of the leaders. As Fig. 18 reveals, the driving speed goes into saturation of 7920 rpm. However, after turning, the vessel, and wind, waves, and current are moving in the same direction. Therefore, the vessel is able to catch up with the leaders and again take its place in the formation. This test shows that even in rough environments, the controller works in a reliable manner. However, safe operation is not assured if the required actuator outputs are larger than what the vessel's actuator are able to provide, because in these situations, the vessel may not be able keep its position in the formation and may collide with other vessels in the formation. Figure 19, which shows the formation parameters, confirms the above discussion.

The state of the CG as well as the position of the control point p of the vessel for this test is presented in Fig. 20. Figures 20(a) and (b) show that the vessels performed a circular motion, as evident by the sinus-shaped trajectory. The vessel starts towards North ($\theta = 0$ deg) and turns counterclockwise towards West, South, East, and North again (Fig. 20c). As explained, the follower vessel cannot catch up with the leaders due to the strong disturbances in a portion of the motion; however, after turning and seeing the disturbances from the back, the follower does regain the proper formation. Therefore, the forward speed u is not constant over time (Fig. 20d). The lateral local speed component v is large while the vessel perceives the disturbances from port (approximately the first 40 s). In this situation, both the actuators as well as disturbances are contribut-

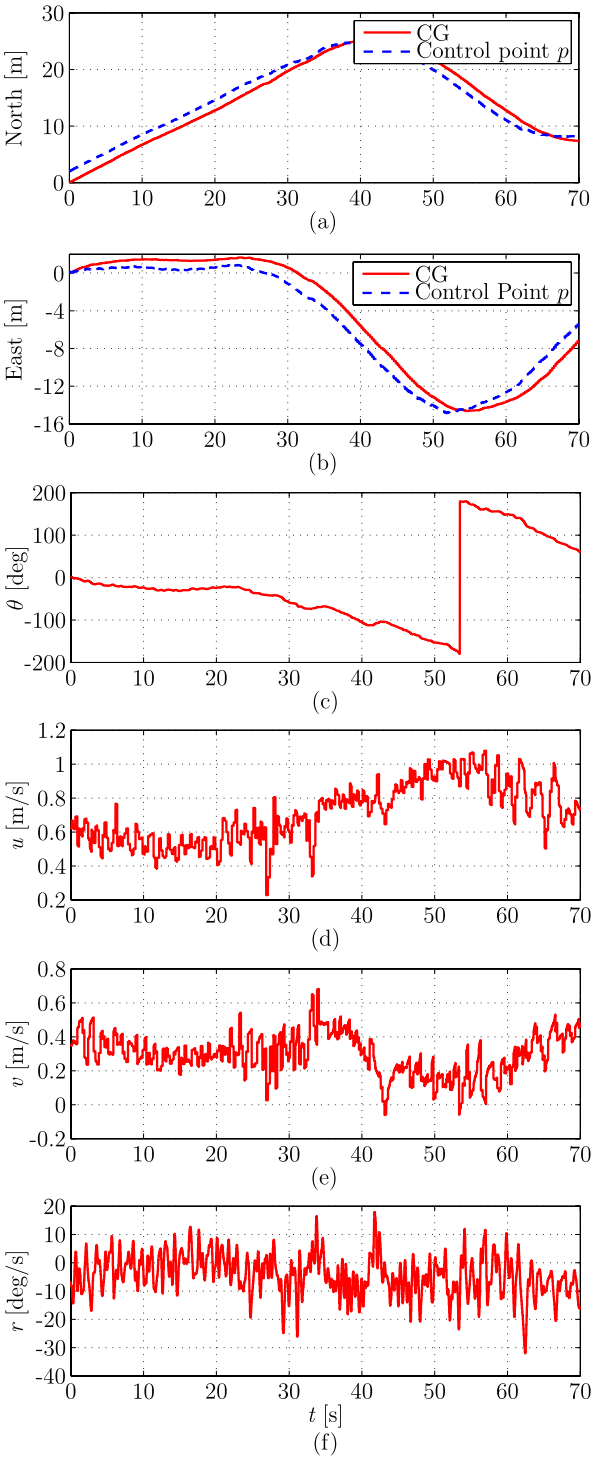

Fig. 20 Circular motion: state of the center of gravity of the vessel (sliding mode controlled)

ing to the lateral speed component. After the vessel experienced the disturbances from starboard, they are counteracted by the lateral velocity component. This is evident in the lateral velocity component, which is approximately halved (Fig. 20e). As expected, the average angular yaw speed is about -5.7 deg/s but the signal exhibits high noise levels (Fig. 20f).

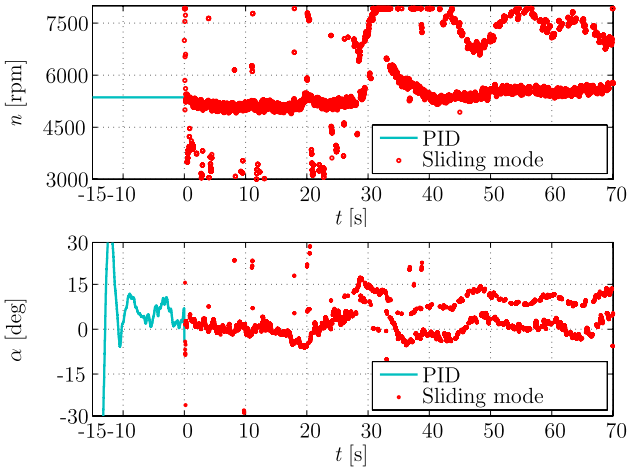

Fig. 21 Zig-zag motion: inputs $[n, \alpha]$

7.3 Zig-zag motion

A zig-zag motion test of the sliding mode controller is presented next. This test is performed in relatively calm waters, so the environmental disturbances are small. The vessel is moving steadily while controlled by the PID controller; i.e., $\dot{v} \approx 0$ and $r \approx 0$. Further, at the steady-state, Fig. 21 shows $n = 5250$ rpm, and $\alpha = 3$ deg, and Fig. 24(e) reveals $v = 0.05$ m/s at the time $t = 0$. Therefore, the total disturbances are estimated by the use of the second dynamic (3) as

$$w \approx w_v = d_{22}v - Y$$
$$= d_{22}v - 2\rho D^4 K_t n|n| \sin\alpha = 0.8 \text{ N}, \quad (53)$$

which represents 4% of the maximal driving force of approximately 20 N. In order to obtain a zig-zag course for the leaders with a constant forward speed u and no lateral motion v, a seven-order polynomial was used to describe the leader's motion. Figure 22 presents the trajectory of the leader-follower formation. The follower followed the leaders with a small deviation. This deviation remained small during operations. The desired and the actual output values for l_{13} and l_{23} during the test are shown in Fig. 23. The vessel is not able to fully catch up with the leaders, when they are changing from a North-East movement to a North-West movement, due to the Eastward disturbances. The inputs are presented in Fig. 21. This test is performed with a moderate value of the chattering parameter; i.e., $\phi = 0.2$. Chattering is still present.

The state of the CG of the vessel as well as the position of the control point p of the vessel for this test are as expected, and are shown in Fig. 24. As mentioned previously,

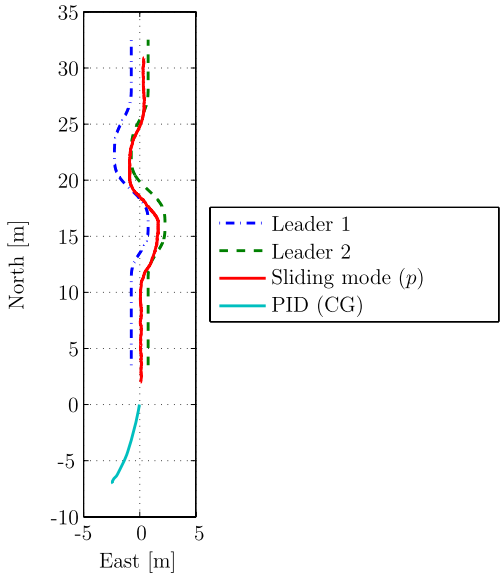

Fig. 22 Zig-zag motion: trajectory

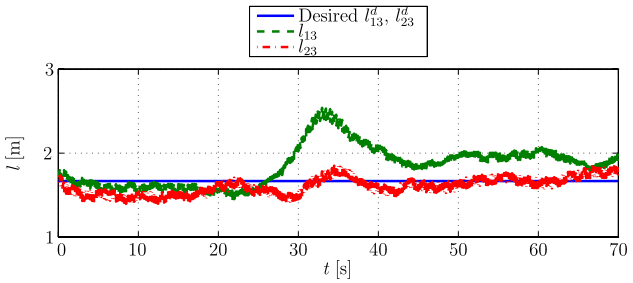

Fig. 23 Zig–zag motion: comparison of the desired values l_{13}^d and l_{23}^d and the actual outputs l_{13} and l_{23}

it is evident that the follower is not able to catch up when the leaders when they are changing direction from a North-East movement to a North-West movement. The CG of the vessel is moving on a zig-zag course towards North, with some movement towards East and West. Due to the presence of Eastward disturbances, the CG moves much more towards the East as towards the West (Figs. 24a and b). Due to the disturbances from the port side, the vessel turns its heading angle yaw more towards West to resist the Eastward disturbances (Fig. 24c). The forward speed u reaches its steady state quickly; however, as mentioned the vessel is not able to follow fully (Fig. 24d). Therefore, the vessel had to accelerate, as the peak of the forward speed around $t = 35$ s reveals. Compared to the disturbances for the other tests reported in this paper, the disturbances in this experiment are small; therefore, the lateral speed component remains very small (Fig. 24e). As a zig-zag motion involves a change of the heading yaw θ, the angular change rate is different from zero (Fig. 24f).

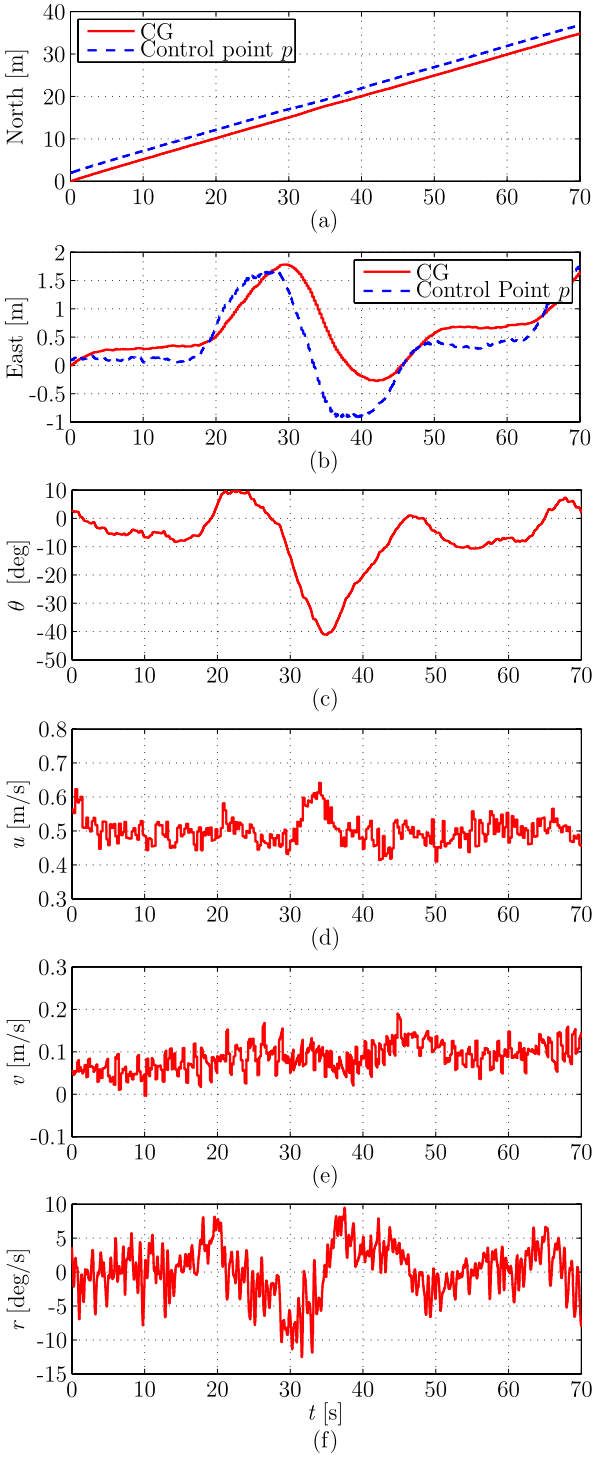

Fig. 24 Zig-zag motion: state of the center of gravity (sliding mode controlled)

8 Conclusion

A nonlinear robust model-based formation controller for marine surface vessels is implemented and experimentally tested. The vessel is assumed to have a planer motion on the

surface of the water with three degrees-of-freedom (DOF) surge, sway, and yaw. Additionally the vessel only has two actuators; and is, thus, underactuated. The zero-dynamics stability for the test vessel is derived to complement the stability criteria for the controller. A leader-follower scheme for formation control is used. Computer simulations are performed to find initial controller gains, which are fine tuned during field experiments. The experiments are performed using a small autonomous surface vessel in a natural environment on a very large freshwater lake with high disturbances compared to the size of the test vessel. Three test scenarios are defined, in which the controlled follower vessel follows two leaders with prescribed motion (straight line, circular, and zig-zag). The performance of each test scenario is consistent in different trials. The tests have shown the effectiveness and robustness of the control laws in the presence of parameter uncertainty and high environmental disturbances.

Acknowledgements The authors would like to convey their thanks to Matthew Bourassa for design, construction, and assemblage of the housing for the PC/104 embedded computer and the navigational sensors, the Mechanical Engineering Machine Shop personnel for constructing parts required for the housing, and Tania Wood for wiring, assembling, and testing the PC/104 embedded computer and the navigational sensor.

This research would not have been possible without funding provided by the Faculty of Engineering at University of Alberta, and the Canadian Natural Sciences and Engineering Research Council (NSERC).

References

Aguiar, A. P., & Hespanha, J. P. (2003). Position tracking of underactuated vehicles. In *Proceedings of the 2003 American control conference* (Vol. 3, pp. 1988–1993). doi:10.1109/ACC.2003.1243366.

Alves, J., Oliveira, P., Oliveira, R., Pascoal, A., Rufino, M., Sebastiao, L., & Silvestre, C. (2006). Vehicle and mission control of the delfim autonomous surface craft. In *Proceedings of the 14th Mediterranean conference on control and automation* (pp. 282–287), Piscataway, NJ, USA.

Ashrafiuon, H., Muske, K. R., McNinch, L. C., & Soltan, R. A. (2008). Sliding-mode tracking control of surface vessels. *IEEE Transactions on Industrial Electronics*, *55*(11), 4004–4012.

Balch, T., & Arkin, R. C. (1998). Behavior-based formation control for multirobot teams. *IEEE Transactions on Robotics and Automation*, *14*(6), 926–939.

Behal, A., Dixon, W. E., Dawson, D. M., & Fang, Y. (2000). Tracking and regulation control of an underactuated surface vessel with nonintegrable dynamics. In *Proceedings of the IEEE Conference on Decision and Control* (Vol. 47, pp. 2150–2155). Sydney, Australia, December 2000. New York: IEEE Press.

Bhatti, A. I., Spurgeon, S. K., Dorey, R., & Edwards, C. (1999). Sliding mode configurations for automotive engine control. *International Journal of Adaptive Control and Signal Processing*, *13*(2), 49–69.

Bronstein, I. N., & Semendyayev, K. A. (1985). *Handbook of mathematics* (3rd ed.). Frankfurt/Main: Verlag Harri Deutsch.

Dash, P. K., Sahoo, N. C., Elangovan, S., & Liew, A. C. (1996). Sliding mode control of a static VAR controller for synchronous generator stabilization. *International Journal of Electrical Power & Energy Systems*, *18*(1), 55–64.

Desai, J. P. (2002). A graph theoretic approach for modeling mobile robot team formations. *Journal of Robotic Systems*, *19*(11), 511–525.

Duman, H. & Hu, H. (2001). United we stand, divided we fall: Team formation in multiple robot applications. *Journal of Robotic Systems*, *16*(4), 153–161.

Encarnacao, P., & Pascoal, A. (2001). Combined trajectory tracking and path following: an application to the coordinated control of autonomous marine craft. In *Proceedings of the 40th IEEE conference on decision and control* (Vol. 1, pp. 964–969). New York: IEEE Press.

Fahimi, F. (2007a). Sliding-mode formation control for underactuated surface vessels. *IEEE Transactions on Robotics*, *23*(3), 617–622.

Fahimi, F. (2007b). Non-linear model predictive formation control for groups of autonomous surface vessels. *International Journal of Control*, *80*(8), 1248–1259.

Fahimi, F. (2008). Full formation control for autonomous helicopter groups. *Robotica*, *26*(2), 143–156.

Fahimi, F., Rineesh, S. V. S., & Nataraj, C. (2008). Formation controllers for underactuated surface vessels and zero-dynamics stability. *Control and Intelligent Systems*, *36*(3), 277–287.

Fossen, T. I. (1994). *Guidance and control of ocean vehicles*. Chichester: Wiley.

Gyoungwoo, L., Surendran, S., & Kim, S.-H. (2009). Algorithms to control the moving ship during harbour entry. *Applied Mathematical Modelling*, *33*(5), 2474–2490.

Indiveri, G., & Aicardi, M. (2000). Nonlinear time-invariant feedback control of an underactuated marine vehicle along a straight course. In *Proceedings of 5th IFAC conference on maneuvering and control of marine craft* (pp. 221–226).

Innocenti, M., & Campa, G. (1999). Robust control of underwater vehicles: sliding mode vs. LMI synthesis. In *Proceedings of the 1999 American control conference* (Vol. 5, pp. 3422–3426), San Diego, CA, USA.

Kapila, V., Sparks, A. G., Buffington, J. M., & Yan, Q. (1992). Spacecraft formation flying: Dynamics and control. *Journal of Guidance, Control, and Dynamics*, *23*, 561–564.

Lewis, M. A., & Tan, K.-H. (1997). High precision formation control of mobile robots using virtual structures. *Autonomous Robots*, *4*, 387–403.

Naeem, W., Sutton, R., Chudley, J., Dalgleish, F. R., & Tetlow, S. (2005). An online genetic algorithm based model predictive control autopilot design with experimental verification. *International Journal of Control*, *78*(14), 1076–1090.

Naeem, W., Xu, T., Sutton, R., & Tiano, A. (2008). The design of a navigation, guidance, and control system for an unmanned surface vehicle for environmental monitoring. *Journal of Engineering for the Maritime Environment*, *222*, 67–79. Proceedings of the institution of mechanical engineers part M.

Pettersen, K. Y., & Egel, O. (1997). Robust control of an underactuated surface vessel with thruster dynamics. In *Proceedings of 1997 American control conference* (pp. 3411–3416).

Pettersen, K. Y., & Nijmeijer, H. (1998). State tracking control of an underactuated surface vessel. In *Proceedings of the 37th IEEE conference on decision and control* (pp. 4561–4566). New York: IEEE Press.

Proca, A. B., Keyhani, A., & Miller, J. M. (2003). Sensorless sliding-mode control of induction motors using operating condition dependent models. *IEEE Transactions on Energy Conversion*, *18*(2), 205–212.

Roberts, G. N. (2008). Trends in marine control systems. *Annual Reviews in Control*, *32*(2), 263–269.

Sheikholeslam, S., & Desoer, C. A. (1992). Control of interconnected nonlinear dynamical systems: The platoon problem. *IEEE Transactions on Automatic Control*, *37*(6), 806–810.

Slotine, J.-J. E., & Li, W. (1991). *Applied nonlinear control*. Upper Saddle River: Prentice Hall.

SNAME (1950). Nomenclature for treating the motion of a submerged body through a fluid. *Technical and research bulletin* (1–5). Society of Naval Architects and Marine Engineers.

Sugar, T., & Kumar, V. (1998). Decentralized control of cooperating mobile manipulators. In *Proceedings of IEEE international conference on robotics and automation* (pp. 2916–2921), Leuven, Belgium.

Tsaprounis, C. J., & Aspragathos, N. A. (1999). Sliding mode with adaptive estimation force control of robot manipulators interacting with an unknown passive environment. *Robotica*, *17*, 447–458.

Vaneck, T. W. (1997). Fuzzy guidance controller for an autonomous boat. *IEEE Control Systems Magazine*, *17*(2), 43–51.

Daniel Schoerling received his MSc in Mechanical Engineering and his MBA from the Technische Universiät Bergakademie Freiberg, Germany. He has enhanced his studies in Argentina, New York, USA and Alberta, Canada. Currently, he is performing his PhD studies at the European Organization for Nuclear Research (CERN) in Geneva, Switzerland.

Chris Van Kleeck received his Masters of Science from the University of Alberta in November of 2009. He received his Bachelor of Applied Science in Engineering Physics at the University of British Columbia in 2004. His research interests include robotic simulations, autonomous planning algorithms, and multi-robot systems.

Farbod Fahimi is an Assistant Professor at the University of Alabama in Huntsville, AL, USA. His research interest includes robotics, autonomous vehicles, and nonlinear control. He received his MSc and PhD degrees in Mechanical Engineering form Sharif University of Technology in 1994 and 1999, respectively.

Charles Robert Koch received his BS degree in mechanical engineering from the University of Alberta, Edmonton, Canada in 1985, and his MS and PhD degrees from Stanford University, Palo Alto, CA, in 1986 and 1991, respectively. From 1991 to 1992 and from 1994 to 2001 he worked at Daimler-Benz–DaimlerChrysler in Stuttgart Germany in advanced internal combustion engines. During 1992 to 1994 he worked for General Motors. In 2001, he joined the Mechanical Engineering Department of the University of Alberta, Edmonton Canada, where he is a Professor. His research interests include combustion engines, advanced powertrains and control of fluid systems.